

Landslides (2021) 18:2835–2853
 DOI 10.1007/s10346-021-01682-w
 Received: 3 September 2020
 Accepted: 26 April 2021
 Published online: 11 May 2021
 © Springer-Verlag GmbH Germany
 part of Springer Nature 2021

Jianxian He · Shengwen Qi · Zhifa Zhan · Songfeng Guo · Chunlei Li · Bowen Zheng · Xiaolin Huang · Yu Zou · Guoxiang Yang · Ning Liang

Seismic response characteristics and deformation evolution of the bedding rock slope using a large-scale shaking table

Abstract Qinghai-Tibet Plateau is one of the most seismically active areas of China and rock mass structures or geological structure are also complex here. Earthquake-induced geological disasters are occurred frequently in this region. Among them, plane failure is often generated on bedding rock slope especially in destructive area of the Wenchuan earthquake which caused numerous casualties and serious economic loss. To reveal failure mechanism of bedding rock slope, this paper studied the seismic response and investigated progressive failure characteristics of the bedding rock slope through a large-scale shaking table test. A bedding rock slope of 45° contained an unfilled joint set with spacing of 0.1 m that dipped at an angle of 34° out of the surface, was conducted in a rigid model box, with a length of 3.47 m, width of 0.68 m, and height of 1.2 m, respectively. A series of tests results show that acceleration amplification factor in horizontal direction (AAF-X) increases with the increase of the slope elevation and acceleration amplification factor in vertical direction (AAF-Z) amplifies at lower part of the slope. When the shaking intensities are over 0.2 g, the slope crest and its vicinity start to show nonlinear dynamic response. Existence of bedding planes let the isoline morphology of AAF-X redistribute and dominate the seismic amplification at the crest. The progressive failure progress of the model under earthquake can be divided into four stages. This novel experiment offers some important insights to mechanism of bedding plane landslides triggered by earthquakes, evaluation stability of slopes under earthquake, and disaster prevention and mitigation.

Keywords Shaking table test · Bedding rock slope · Progressive failure · Seismic response

Introduction

In recent decades, earthquake-induced landslides caused numerous casualties and enormous economic loss, e.g., on May 12, 2008 the Wenchuan earthquake triggered landslides lead to 20,000 deaths directly (Qi et al. 2010; Yin et al. 2009). Among these coseismic landslides, the failure of bedding rock slope whose weak structures dip out of the slope surface (Hoek and Bray 1981), was noteworthy and catastrophic, because of suddenly sliding, high velocity and substantial volume. For example, the Tangjiashan landslide (Qi et al. 2015; Xu et al. 2013), Donghekou landslide (Qi et al. 2011; Wang et al. 2014) and Wenjiagou landslide (Zhang et al. 2016) caused by the Wenchuan earthquake. Also, Tsaoling landslide (Chigira et al. 2003) and Chiufengershan landslide (Shou and Wang 2003; Wang et al. 2003), triggered by Chi-Chi earthquake in 1999. Thus, the study on seismic response of a bedding rock slope is primarily necessary to reveal the mechanism and mitigate the damage of landslide disaster of this kind coseismic disaster.

To evaluate the seismic response and investigate the progressive failure evolution of a slope, field observation, numerical simula-

tion, theoretical analysis and physical modeling are widely adopted in rock slope engineering. Field observations indicate that peak ground motion acceleration (PGA) is amplified at the crest of slope (Davis and West 1973; Finn et al. 1995; Wang et al. 2017), and the surficial sediment, weathered rock mass and discontinuities have a significant influence on seismic response characteristics (Bouchon and Barker 1996; Graizer 2009; He et al. 2020; Pelekis et al. 2017; Qi et al. 2012). Meanwhile, the effect of input frequency, incidence angle and geometry on seismic response of slope have been discussed by the Fast Lagrangian Analysis of Continua method with the code FLAC (Bouckovalas and Papadimitriou 2005; Qi et al. 2003; Zhan and Qi 2017; Zhang et al. 2018). The discrete element method (DEM) code UDEC has been undertaken to study the deformation characteristics of the slope under earthquake excitation (Bhasin and Kaynia 2004; Li et al. 2019c). Furthermore, two analytical solutions have been reached to evaluate the stability of the dip slope (Qi et al. 2015) and the antidip slope (Guo et al. 2017), respectively. Nevertheless, it is often difficult to quantitatively investigate rock mass structure or geometry impact on seismic response of a slope. Up to now, there is no numerical simulation method and theoretical analysis that can completely reveal the seismic response of a practical slope, due to complicated constitutive relation and nonlinear dynamic response.

Besides the methods mentioned above, physical modeling, e.g., shaking table test can predesign the rock mass structure and slope geometry. Through digital image correlation (DIC) and time-frequency signal analysis (Fan et al. 2017; Song et al. 2018b; Yan et al. 2020), it can directly reveal the seismic response characteristics and distinguish the failure mode or progressive failure evolution, under different types of earthquake waves. Wartman et al. (2005) found that soil slope showed a nonlinear seismic response and permanent deformation varied along the length of the models. Through a series of shaking table tests, Lin and Wang (2006) and Wang and Lin (2011) found that the acceleration amplification of homogenous soil slopes at the crest appeared to be quite significant and the failure surface appeared to be shallow. They also concluded that the failure of a slope can be defined from a corresponding acceleration record displaying significant nonlinear seismic response after crack initiation. Liu et al. (2013) found that the acceleration amplification factor in horizontal direction increased with the slope elevation, while the acceleration amplification factor in vertical showed a lying shaped changing pattern by the means of shaking table test. Liu et al. (2014) also found that the layered model slope produced the larger acceleration amplification factor than the homogeneous model slope and the upper half of a slope was influenced more seriously by the effect of lithology, through a series of shaking table tests. The surface displacement of the bedding slope was greater than that of the counter-bedding slope, and the counter-bedding slope was more stable compared to the bedding slope, under same input excitation (Fan et al. 2016). In addition, seismic stability of a

bedding and a counter-bedding slope using the time-frequency method were proposed by shaking table tests (Fan et al. 2017; Fan et al. 2019). A series of small-scale shaking table tests revealed that initial deformation occurred at the slope crest and massive movement of the rock mass was along the weak plane, and larger dip angle of the slope or higher slope height tended to shorten the duration of dip slope deformation (Li et al. 2018). Li et al. (2019b) and Li et al. (2019c) found that the sliding surface of a bedding slope was nearly parallel to the slope surface while that of a counter-bedding was skewed the bedding planes, and the surface location was related to dip and spacing of the bedding planes. Shaking table test results showed that acceleration would suddenly increase above the bedding plane and the settlement deformation and sliding deformation were induced by the P waves and S waves, respectively (Song et al. 2018a; Song et al. 2018b). Furthermore, some papers presented researches into effect of antidip plane on dynamic response of slope and recognizing cracks types and topping sliding surface (Huang et al. 2013; Yang et al. 2018).

In summary, previous studies addressed that rock mass discontinuities had a significant effect on seismic response and failure mechanism of the slopes. More attentions have been paid for homogenous slopes and slopes with simple joint set under the excitation with a narrow range of frequencies. In addition, the size of the slope models was also small and the bedding planes were commonly treated as filled joints, as summarized in Table 1. Nevertheless, postearthquake investigations showed that consequent slopes had a higher landslides incidence than other layered slopes and original slopes of rock slopes concentrated in 30–40° (Qi et al. 2010), e.g., Tangjiashan landslide (Qi et al. 2015) and Donghekou landslide (Yuan et al. 2014). More importantly, strata slopes of the bedding planes of some catastrophic earthquake-induced landslides were between 30° and 40° which were smaller than the inclination angle of the original slope, e.g., Chiufengershan landslide on the downslope (36°) and Wenjiagou landslide (35°) (Wang et al. 2003; Zhang et al. 2016). Hence, to reveal mechanism of this kind geohazard, this study conducts a 45° slope with an unfilled joint set that dips at an angle of 34° out of the surface with spacing of 0.1 m, and the length, width, and height of the model are 3.47 m, 0.68 m, and 1.2 m, respectively. Then, the seismic response of the slope is investigated with a series of shaking table tests under different earthquake recordings and sinusoidal waves cover a wide frequency range and amplitude and the failure mode of bedding plane slope is detailed. Finally, the acceleration amplification effect on the bedding slope failure pattern is studied. The study provides

some insights into dynamic response characteristics and failure mechanism of the bedding slope under seismic loading.

Shaking table model test

In this study, the 1-g bedding rock model slope was adopted using a large-scale shaking table test to study the seismic response behavior under earthquake. The similarity relations between the prototype and model, experimental facilities, preparation of the model slope, monitoring system and input excitations, are introduced in the following sections.

Similarity relations

Based on the Buckingham π theorem (Buckingham 1914) and similarity three theorems proposed by Brand (1957), the law of similitude was widely applied in static and dynamic aspects of soil or rock materials (Fan et al. 2016; Iai 1989; Lin and Wang 2006; Liu et al. 2013; Meymand 1998). To obtain similitude equations, key influence factors are determined first, then dimensional analysis is carried out according to the Buckingham π theorem (Buckingham 1914), and similarity criterion is derived finally (Brand 1957; Curtis et al. 1982). In this study, thirteen parameters are considered and those parameters should satisfy the following physical function:

$$f(l, \rho, a, E, c, \phi, \sigma, \varepsilon, u, v, t, f, g) = 0 \quad (1)$$

where, l denotes the length, ρ the density, a the acceleration, E elasticity modulus, c the cohesion, ϕ the internal friction angle, σ stress, ε strain, u the displacement, v the velocity, t the time, f frequency, and g gravitational acceleration. To simplify the needs of scaling of parameters in the 1-g model test, the material density ρ of the model and prototype are keeping the same proposed by Wang and Lin (2011).

Variables in Eq. (1) can be expressed using three fundamental dimensions, i.e., length [L], time [T] and mass [M]. Table 2 lists dimensions involved in the current study.

Based on dimensional consistency, we can have the following equation by combining each term:

$$M^0 L^0 T^0 = L^{a_1} \cdot (ML^{-3})^{a_2} \cdot (LT^{-2})^{a_3} \cdot (ML^{-1}T^{-2})^{a_4} \cdot (ML^{-1}T^{-2})^{a_5} \cdot (1)^{a_6} \cdot (ML^{-1}T^{-2})^{a_7} \cdot (1)^{a_8} \cdot (L)^{a_9} \cdot (LT^{-1})^{a_{10}} \cdot (T)^{a_{11}} \cdot (T^{-1})^{a_{12}} \cdot (LT^{-2})^{a_{13}} \quad (2)$$

Table 1 Bedding rock slope shaking table test from previous studies

Researchers	Slope model size (length × height)	Slope angle	Bedding plane angle	Bedding plane characteristics
Yang et al. (2012)	1.45 m × 1.6 m	60°	25°	Mixture of rosin and alcohol
Liu et al. (2014)	1.5 m × 1.5 m	60°	0°	3-mm thick fine sands
Fan et al. (2016)	1.7 m × 2.0 m	72°	8°	3-cm thick similar material
Li et al. (2018)	12, 18, and 24 layers (corresponding to 0.06, 0.09, and 0.12 m)	0°, 15°, 25°, and 30°	0°, 15°, 25°, and 30°	Artificial rock balls, polyvinyl acetate (also known as resin)
Li et al. (2019b)	1.5 m × 1.7 m	65°	65°	Infill similar material

Table 2 Dimensions of considered parameters in our shaking table test (a_i is the i -th parameter's exponential term)

	l a_1	ρ a_2	a a_3	E a_4	c a_5	ϕ a_6	σ a_7	ε a_8	u a_9	v a_{10}	t a_{11}	f a_{12}	g a_{13}
[M]	0	1	0	1	1	0	1	0	0	0	0	0	0
[L]	1	-3	1	-1	-1	0	-1	0	1	1	0	0	1
[T]	0	0	-2	-2	-2	0	-2	0	0	-1	1	-1	-2

Based on Eq. (2), we can have Eq. (3).

$$\begin{cases} a_2 + a_4 + a_5 + a_7 = 0 \\ a_1 - 3a_2 + a_3 - a_4 - a_5 - a_7 + a_9 + a_{10} + a_{13} = 0 \\ -2a_3 - 2a_4 - 2a_5 - 2a_7 - a_{10} + a_{11} - a_{12} - 2a_{13} = 0 \\ a_6 + a_8 = \text{constant} \end{cases} \quad (3)$$

Meanwhile, soil density ρ , geometric dimension l , and acceleration a were selected as the fundamental variables. Hence, on the basis of three fundamental variables, Eq. (1) can be transferred to the following equation.

$$F(\pi_1, \pi_2, \pi_3, \dots, \pi_{10}) = 0 \quad (4)$$

where, π_i the dimensionless similarity criterion.

From Eq. (3) and Eq. (4), the general similarity criterion can be written as:

$$\pi_i = [l]^{a_1} \cdot [\rho]^{a_2} \cdot [a]^{a_3} \cdot [E]^{a_4} \cdot [c]^{a_5} \cdot [\phi]^{a_6} \cdot [\sigma]^{a_7} \cdot [\varepsilon]^{a_8} \cdot [u]^{a_9} \cdot [v]^{a_{10}} \cdot [t]^{a_{11}} \cdot [f]^{a_{12}} \cdot [g]^{a_{13}} \quad (5)$$

Based on the matrix method, the specific similarity criterion for each π can be gotten in Table 3. Meanwhile, soil density ρ , geometric dimension l , and acceleration a were selected as the fundamental variables, and the corresponding scaling factor between the prototype and model are $S_\rho = 1$, $S_l = 100$, $S_a = 1$, respectively. Furthermore, similarity criteria of parameters and corresponding similarity ratios are also listed in Table 3, through the matrix method (Fan et al. 2016).

Shaking table facility

A series of physical tests have been conducted on a three-dimensional and six degrees of freedom shaking table at Earthquake Engineering Research Center, China Institute of Water Resources and Hydropower Research, as shown in Fig. 1. The shaking table has a length of 5 m and a width of 5 m with a full load capacity of 20,000 kg and the excited frequency ranging from 0.1 to 120 Hz. The maximums acceleration under full load in X, Y, and Z direction are 1.0 g, 1.0 g, and 0.7 g, respectively, driven by 7 servo-controlled hydraulic actuators.

Model preparation

The rock slope layers were constructed with prefabricated cubic blocks with a dimension of 10 cm \times 10 cm \times 10 cm, and the cubic blocks were cut to irregular-shaped polygon at the base and surface of the slope. The model material was a mixture of barite powder, quartz sand, gypsum powder, glycerol, and water, with weight proportion of 51.9:34.6:6.0:2.0:5.5, determined by orthogonal experiment (Zhan et al. 2019a). Meanwhile, different laboratory tests were conducted, including uniaxial compression test, splitting test and direct shear test, and some typical test results

are shown in Fig. 2. Thus, appropriate physical and mechanical parameters of the similarity materials could be achieved and are shown in Table 4. Similar to previous study (Liu et al. 2013), the similarity material was used to simulate layered hard rocks, like limestone or sandstone. Furthermore, the bedding plane was simulated by plastic membrane and gypsum powder, and the mechanical parameters are also shown in Table 4.

The slope model was prepared in a rigid steel model box, with a length of 3.57 m, width of 0.7 m, and height of 1.25 m. A total of 24 bedding planes with angle of 34° dipped out of the slope were designed, and the slope angle was set to 45°, as shown in Fig. 3.

Reference grids and lines were marked at the acrylic sheet in preconstruction. When one layer of the strata was finished, the gap between the outline of the model and reference line would be confirmed with a laser horizon. Then, the geometric morphology could be calibrated using a small angle grinder, to guarantee the precision between design and model less than 1 mm. After the manufacturing process, the model was set in a constant temperature and humidity environment for one week before shaking table test. Hence, the weight and physical and mechanical properties of the material would be stable and meet the design value. The final model is shown in Fig. 4.

In the test, an absorber material damping liquid composed of polymers silicone rubber with a shear viscosity of 7.0×10^3 Pa·s, was injected into the gap between model and box, to simulate the radiational damping boundary proposed by Wang et al. (2004). It had been concluded that the tangential damping liquid could adsorb most part of energy transmitted into unbounded medium. Hence, “reasonably correct” test results could be obtained under this condition (Wartman et al. 2005). Furthermore, Lin and Wang (2006) found that the boundary would not affect the location of the sliding surface when the distance of the slope crest to the boundary (in this study is 1.97 m) was equal to or greater than twice the horizontal projected slope length (in this study is 0.9 m). Hence, the geometry of the model also conformed to the criterion proposed by Lin and Wang (2006).

Monitoring system

In order to obtain the dynamic response behavior of the slope, a monitoring system was set up to collect acceleration and displacement data inside and at the surface of the slope. Twenty-seven three-component accelerometers (named as A02, A03, ..., A28) were set at different elevations inside the model and at the surface along the middle line from toe to the top. Another one accelerometer (A01) was mounted on the shaking table to monitor the input motion, as shown in Fig. 3. A triaxial accelerometer (ULT2061) was used in the test made by Lance Technologies, Inc. Each accelerometer had the capacity of up to 5.0 g, frequency response ranging from 0.1 to 1000 Hz and

Table 3 The similarity criterion based on the matrix method

	E a_4	C a_5	ϕ a_6	σ a_7	ε a_8	u a_9	v a_{10}	t a_{11}	f a_{12}
π_1	1	0	0	0	0	0	0	0	0
π_2		1	0	0	0	0	0	0	0
π_3			1	0	0	0	0	0	0
π_4				1	0	0	0	0	0
π_5					1	0	0	0	0
π_6						1	0	0	0
π_7							1	0	0
π_8								1	0
π_9									1
π_{10}									

	g a_{13}	l a_1	ρ a_2	a a_3	Equations	Similarity criterion	Similarity ratios
π_1	0	-1	-1	-1	$\pi_1 = E/(l\rho a)$	$C_E = C_l C_\rho C_a$	$C_E = 100$
π_2	0	-1	-1	-1	$\pi_2 = c/(l\rho a)$	$C_c = C_l C_\rho C_a$	$C_c = 100$
π_3	0	0	0	0	$\pi_3 = \phi$	1	$C_\phi = 1$
π_4	0	-1	-1	-1	$\pi_4 = \sigma/(l\rho a)$	$C_\sigma = C_l C_\rho C_a$	$C_\sigma = 100$
π_5	0	0	0	0	$\pi_5 = \varepsilon$	1	$C_\varepsilon = 1$
π_6	0	-1	0	0	$\pi_6 = u/l$	$C_u = C_l$	$C_u = 100$
π_7	0	-1/2	0	-1/2	$\pi_7 = v/(la)^{1/2}$	$C_v = C_l^{1/2} C_a^{1/2}$	$C_v = 10$
π_8	0	-1/2	0	1/2	$\pi_8 = t(a/l)^{1/2}$	$C_t = C_l^{1/2} C_a^{-1/2}$	$C_t = 10$
π_9	0	1/2	0	-1/2	$\pi_9 = f(a/l)^{-1/2}$	$C_f = C_l^{-1/2} C_a^{1/2}$	$C_f = 0.1$
π_{10}	1	0	0	-1	$\pi_{10} = g/a$	$C_g = C_a$	$C_g = 1$

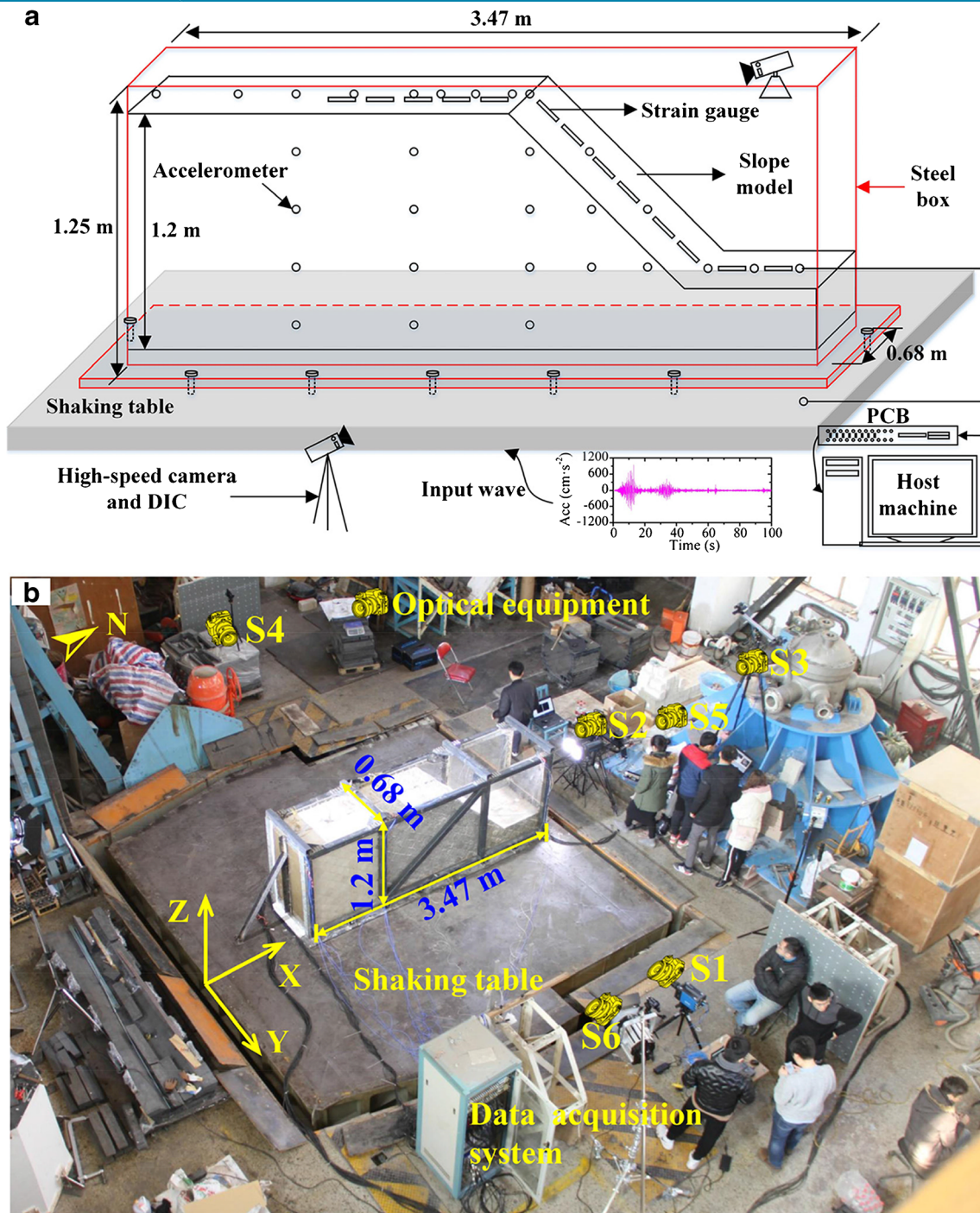


Fig. 1 Physical model design **a** design map for the overall test equipment and **b** layout of the test model and data acquisition equipment (note: S1, S2, ..., S6 represent digital image correlation systems)

with a sensitivity about 1000 mV/g. Resistance strain gauges were placed at surface location of the bedding planes, to measure small displacement and detect the location of crack initiation during test. Additionally, multichannel piezoelectric sensor signal conditioners, manufactured by PCB Piezotronics, Inc, were adopted to record, filter, and analyze acceleration and strain signals, as shown in Fig. 1.

The seismic response deformation behaviors of the model were recorded by a high-speed camera through digital image correlation systems including VIC-3D and VIC-2D supplied by Ruituotech company, which were proved by Liu et al. (2020) and Shi et al. (2015). Six VIC systems, named as S1, ..., S6 including total of 9 optical cameras were used to capture displacement data from different perspectives, as shown in Fig. 1. A Pco.dimax s1 camera

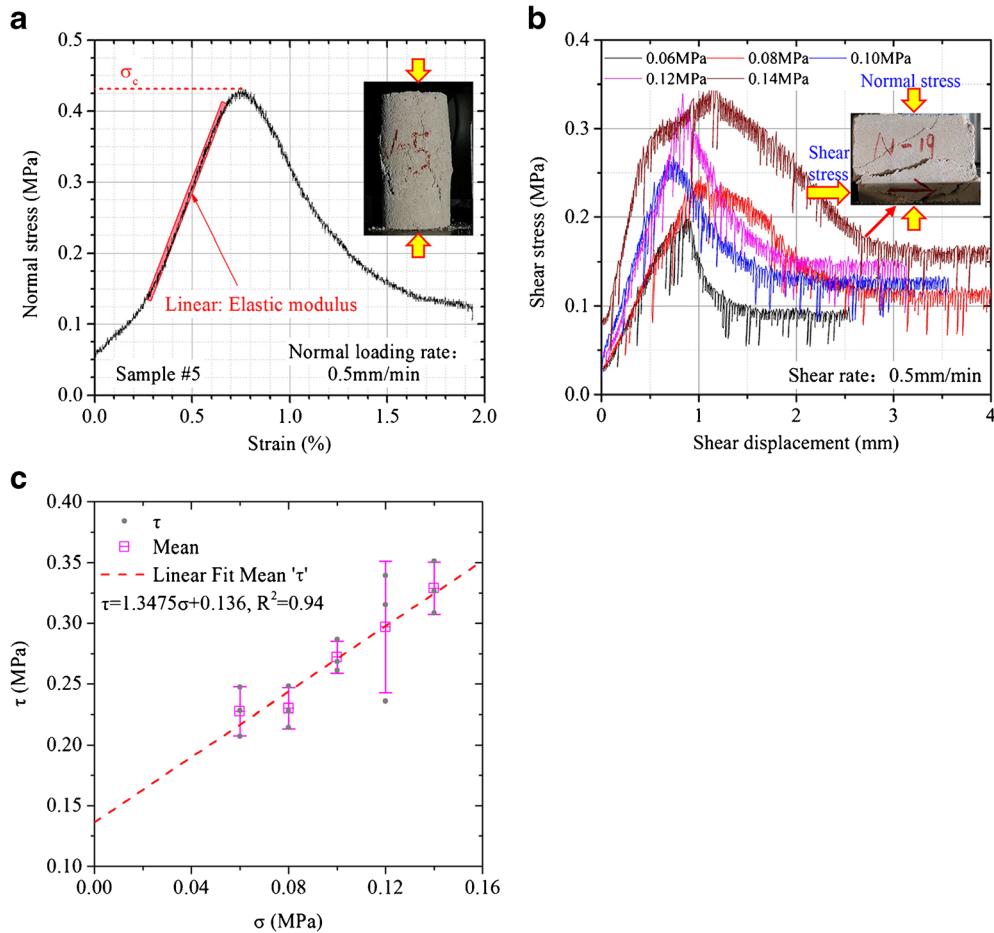


Fig. 2 a Typical uniaxial compression and b direct shear test under different normal stress for the similarity materials, where σ_c represents compression strength. Internal friction angle ϕ and cohesion c are obtained from linear fitting of σ - τ curve

(S1 in Fig. 1) was placed in the east side of the model, to capture displacement in X-Z coordinate system. The resolution was set to 1008×1008 pixels, and frame rate of the camera was varied from 500 to 1000 frames per second (fps) depending on frequency of the loading wave. One VIC-3D system S2 composed of two FASTCAM Mini UX100 cameras, was to obtain the 3D-deformation of the slope surface, located at the north of the model. The resolution and frame rate of this measurement system were set to 896×896 pixels and 200–500 fps. In addition, another one 3D-deformation measurement (S3 in Fig. 1) composed of two FLIR GS3-U3-123S6M-C cameras were set to observe the displacement behind the slope crest from top view. The resolution and frame rate of this measurement system were set to 4096×3000 pixels and 20 fps. Furthermore, three SONY FDR-AX45 cameras (marked S4, S5,

and S6 in Fig. 1) recorded the progressive failure in different perspectives, with resolution of 1920×1080 pixels and frame rate of 25. Specifications of main monitoring instruments are shown in Table 5.

Input excitations

To simulate seismic wave, the model was excited by a series of acceleration-time history curves at the shaking table base. Different waveforms including the sine wave and field earthquake recording of Wolong station during the 2008 Wenchuan earthquake (WL wave) with different amplitudes, were excited by horizontal direction (X-direction), vertical direction (Z-direction) and combined horizontal and vertical directions (XZ). The input frequencies of sine waves were 20, 30, 40, 50, 70 Hz and their amplitudes

Table 4 Physical and mechanical parameters of similarity materials

	Density ρ (kg/m ³)	Elasticity modulus E (MPa)	Compression strength σ_c (MPa)	Poisson's ratio μ	Cohesion c (kPa)	Internal friction angle ϕ (°)
Rock mass	2450	55.8	0.40	0.20	138	53.0
Bedding plane					0.902	27.8

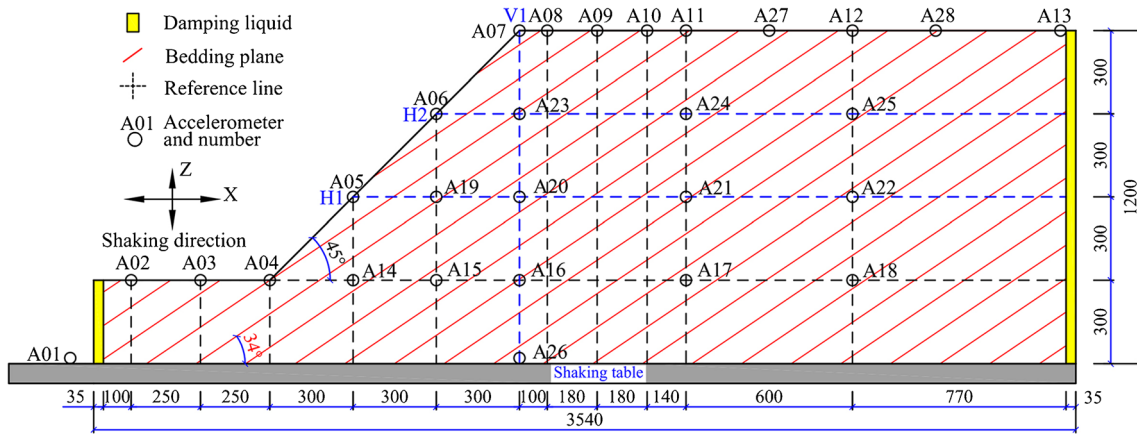


Fig. 3 A sketch of the model slope and layout of the accelerometers (unit: mm). H represents the horizontal direction section, and V represents the vertical direction section

were set to 0.05, 0.10, 0.20, 0.30, and 0.45 g. The east-west (EW) and up-down (UD) components of WL wave are shown in Fig. 5 and they were widely used in physical modeling and earthquake engineering and the detailed site condition description can be found in Liu et al. (2013). Meanwhile, the input amplitudes of WL waves were set to 0.1, 0.2, 0.3, 0.4, 0.5, and 0.7 g proportionally scaled from the PGAs of WL wave. The durations of the input WL waves were also compressed at a ratio of 10, 5, and 1 (R10, R5, R1) to study the effect of frequency content on seismic response. Also, the input original WL (compressed 1 time) was the first 50 s of the records as shown in Fig. 5, because it contained the main energy of the ground motion. Furthermore, the deformation phenomena of the model were investigated and sketched in detail and the validity

of the monitoring data was checked, after each excitation. Finally, a white noise (WN) with an amplitude of 0.05–0.10 g and a frequency range 0.1–120 Hz, was conducted to obtain the dynamic characteristics of the slope model before different type input motions. The detailed scheme of the input excitation (IE) is listed in Table 6.

Results

In this paper, the acceleration amplification factor (AAF) is defined as the absolute value ratio of the peak acceleration recorded by A02, A03, ..., A28 accelerometers to that at the slope toe A04 (Qi et al. 2003), as shown in Fig. 3. Meanwhile, AAF-X denotes the AAF in X direction while the AAF-Z denotes the AAF in vertical

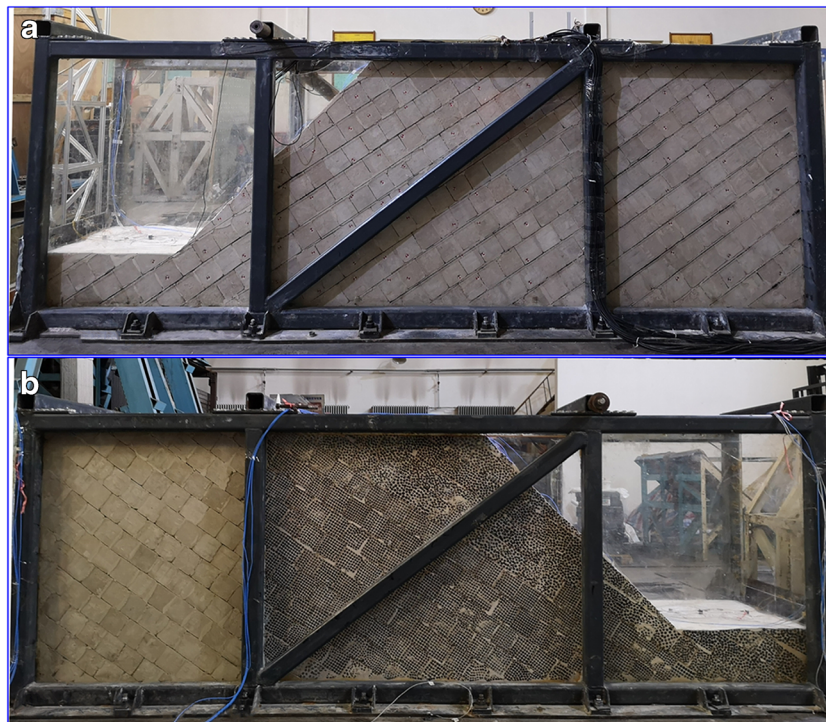


Fig. 4 The final constructed model slope

Table 5 Specifications of instruments used for monitoring

Description	Model	Measurement range	Resolution
Triaxial accelerometer	ULT2061	-5–+5 g	0.00002 g
Digital image correction systems	VIC-2D	Strain range from 0.005 to >2,000%	Strain down to 10 μe ; displacement up to 0.001 pixels
	VIC-3D	Strain range from 0.005 to >2,000%	Strain down to 10 μe ; displacement up to 0.02 pixels

direction, followed the method of Yang et al. (2018). Besides, the normalized height was defined as the ratio of the height of the monitoring point h (h , the corresponding Z coordinates difference between the monitoring point and toe A04) to the height of the model H (H , the corresponding Z coordinates difference between the slope crest monitoring point A07 and toe A04). Hence, the distribution of the AAF can reflect the seismic response of the bedding slope under different types of waves and frequency characteristic.

Acceleration response analysis

The recorded accelerations are first baseline corrected and filtered in the MATLAB 9.5. Butterworth passband filtering is employed with a polynomial of up to the 8th degree and a frequency range varied in different IEs. To better understand the seismic response of the slope, the pseudocolor contour maps of AAF-X under 0.05-g horizontal sine wave excitation, 0.1-g horizontal sine wave excitation, 0.2-g horizontal sine wave excitation, 0.1-g vertical sine wave excitation, 0.1-g vertical WL wave, and 0.1g XZ WL wave are shown in Fig. 6, which indicate significant seismic amplification at and behind the crest. Especially, only results of input amplitudes less than 0.2 g are presented here because the model is approximately in elastic state when input amplitudes are smaller than 0.2 g (Lin and Wang 2006; Liu et al. 2013).

From Fig. 6, AAF-X is amplified with the increase of the slope elevation along the slope surface and reaches its peak value at the

slope crest. Meanwhile, the AAF-X also remains considerable amplification behind the slope crest while slightly smaller than its crest value. The AAF-X also increases with the increase of the excitation amplitudes, as shown in Fig. 6(a), (b), and (c), and the larger the amplitude and the wider the range of the dynamic response amplification area. These phenomena can also be clearly observed from the AAF-X along the surface (A04, A05, A06, A07) and along the vertical direction section V1 (A16, A20, A23, A07), as shown in Fig. 7(a) and (b), respectively. Additionally, the increment of the AAF-X at the crest of the slope also increases with the increase of the input amplitude, which is consistent with the results indicated from an antidipping rock slope shaking table test by Yang et al. (2018). Furthermore, the AAF-X shows an approximately linear increase when the normalized height was smaller than 2/3, while the AAF-X has a sharp or nonlinear increase at the slope crest, as shown in Fig. 7(b). This is mainly because the constraint of the slope crest is smaller than that at the lower part.

Spectrum characteristics of seismic waves, as well as excitation direction, have a profound influence on the seismic response of the slope, which have been recognized from postearthquake disaster investigations and shaking table tests (Collier and Elnashai 2001; Liu et al. 2013; Yin et al. 2009). As shown in Fig. 6(d) and (e) under same excitation direction and amplitude, it can be found that the AAF-X under sine wave excitation is distributed in a wider range at the slope surface than that under WL wave. Besides, the AAF-X under horizontal direction excitations is larger than that under vertical excitation, as illustrated in Figs. 6(b), 6(d), and 8(a). Similarly, the AAF-Z under vertical excitation is larger than that under horizontal excitation. Because the size of the model is equivalent to a rigid body, the vibration of the particle in X-direction under horizontal excitation will be stronger than that under vertical direction in elastic state.

Nevertheless, the AAF-Z gradually increases to its maximum until the normalized height reaches 1/3, unlike the AAF-X at the slope crest, as shown in Fig. 8(a). Meanwhile, the AAF-Z keeps nearly unchanged along the vertical section V1 under WL wave excitation, as shown in Fig. 8(b). Although the step-like slope surface can reduce the overall system stiffness or constraint, the degree of reduction in the horizontal direction is greater than that in vertical. Therefore, the AAF-Z along the surface is smaller than the AAF-X. Furthermore, the AAF-Z will attenuate at a certain height due to combined effect of topography and bedding plane in this study.

Interestingly, the variation of the AAF-X along the horizontal section H2 (A06, A23, A24, A25) also shows different characteristics under different waveforms, as shown in Fig. 9. The AAF-X increases slightly first and then decreases with decreasing horizontal distance from the accelerometer to slope surface under sine wave excitation in Fig. 9(a). Nevertheless, it is indicated that the AAF-X decreases first and then increases with decreasing

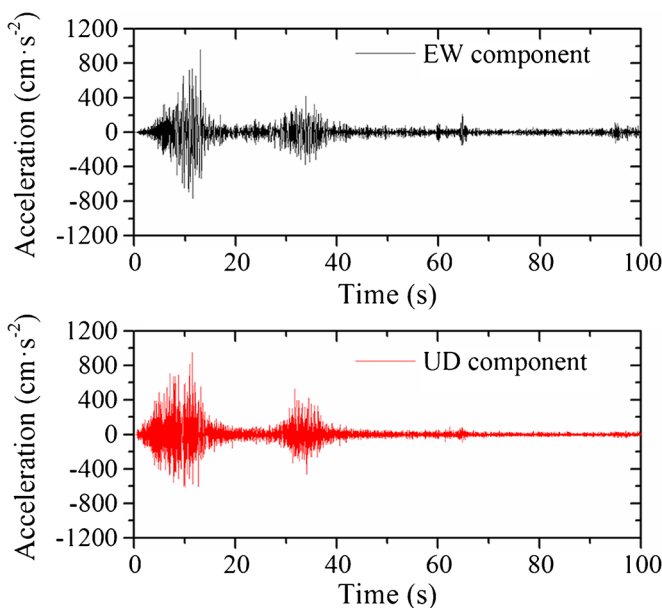
**Fig. 5** Time-history acceleration of WL wave in EW and UD directions

Table 6 The scheme of the input excitations

IE no.	Waveform type	Characteristics of the input motion at the shaking table base.
1	WN-1	White noise. Intensity is 0.05 g.
2–6	Sine wave	X-direction excitation. Intensity is 0.05 g. Frequency is 20, 30, 40, 50, and 70 Hz, respectively.
7	WN-2	White noise. Intensity is 0.05 g.
8–10	WL	XZ-direction excitation. Intensity is 0.10 g. Compressed time is 10, 5, and 1, respectively.
11	WN-3	White noise. Intensity is 0.05 g.
12–14	WL	Z-direction excitation. Intensity is 0.10 g. Compressed time is 10, 5, and 1, respectively.
15	WN-4	White noise. Intensity is 0.05 g.
16–20	Sine wave	Z-direction excitation. Intensity is 0.10 g. Frequency is 20, 30, 40, 50, and 70 Hz, respectively.
21	WN-5	White noise. Intensity is 0.05 g.
22–25	Sine wave	X-direction excitation. Intensity is 0.10 g. Frequency is 20, 30, 40, and 50 Hz, respectively.
26	WN-6	White noise. Intensity is 0.05 g.
27–31	Sine wave	X-direction excitation. Intensity is 0.20 g. Frequency is 20, 30, 40, 50, and 70 Hz, respectively.
32	WN-7	White noise. Intensity is 0.05 g.
33–35	WL	XZ-direction excitation. Intensity is 0.20 g. Compressed time is 10, 5, and 1, respectively.
36	WN-8	White noise. Intensity is 0.05 g.
37	Sine wave	X-direction excitation. Intensity is 0.30 g. Frequency is 20 Hz.
38	Sine wave	X-direction excitation. Intensity is 0.45 g. Frequency is 30 Hz. Rock masses were sliding along the second bedding plane.
39	WN-9	White noise. Intensity is 0.05 g.
40–42	WL	XZ-direction excitation. Intensity is 0.30 g. Compressed time is 10, 5, and 1, respectively.
43–45	WL	XZ-direction excitation. Intensity is 0.40 g. Compressed time is 10, 5, and 1, respectively.
46	WN-10	White noise. Intensity is 0.05 g.
47–49	WL	XZ-direction excitation. Intensity is 0.50 g. Compressed time is 10, 5, and 1, respectively.
50	WN-11	White noise. Intensity is 0.05 g.
51–52	WL	XZ-direction excitation. Intensity in horizontal and vertical are 0.70 g and 0.50 g, respectively. Compressed time is 5.
53	WN-12	White noise. Intensity is 0.05 g.
54–55	Sine wave	X-direction excitation. Intensity is 0.45 g. Frequency is 30 Hz.

horizontal distance from the accelerometer to slope surface under WL wave excitation, as shown in Fig. 9(b). Hence, seismic response of the slope is affected greatly by input motion characteristics. This is caused by interaction between resonance frequency of the model and input motion spectral characteristics.

Deformation characteristics

Based on multisource data collected from high-speed photos, strain gauge and monitoring acceleration, the deformation and progressive failure process of the model slope can be summarized into four stages as follows. For the sake of narrative, the bedding planes are numbered from top to bottom as shown in Fig. 10.

Stage I: when the input amplitudes of the acceleration are less than 0.2 g, no obvious deformation occurs and only a few tensional cracks initiate between the blocks at the crest of the slope along bedding planes of No.1 and No.2 primarily, as shown in Fig. 10. Those tensional cracks are parallel to the

strike direction of the joint, with lengths of ~6–8 cm. Also, apertures of those cracks are less than 0.1 mm by hand magnifier framed in a circular area in Fig. 10.

Stage II: as the input amplitudes of the acceleration are 0.3 g, existing tensional cracks continue to grow and several new tensional cracks are observed at the crest of the slope along bedding planes of No.1 and No.2, as shown in Fig. 11. Meanwhile, several shear cracks with a length of about 5 cm present at the slope surface above one-third of the slope height along bedding planes of No.1 and No.2, due to the differential deformation among blocks, marked dashed line in photo as seen in Fig. 11.

Stage III: when the shaking amplitude of the acceleration reaches 0.45 g (input excitation IE38 in Table 6), lots of cracks take place, especially in the region above No.2 bedding plane, crack distributed region is dramatically expanded, and the farthest crack occurs in the seventh layer (between bedding plane No.6 and No.7), as shown in Fig. 12(a). Cracks grow

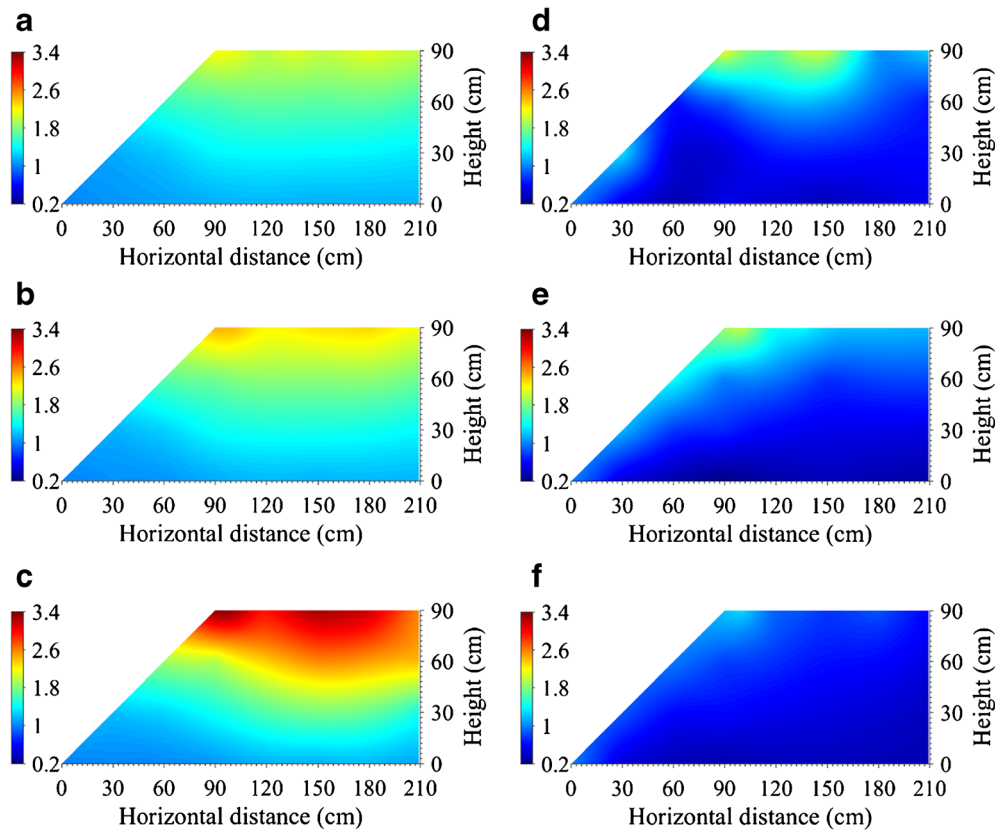


Fig. 6 The contour map of AAF-X: a, b, and c horizontal 30 Hz sine wave excitation with varied amplitudes of 0.05 g, 0.1 g, and 0.2 g, respectively; d vertical 30 Hz sine wave excitation with amplitude 0.1 g; e 0.1 g vertical WL wave; f 0.1 g XZ WL wave (compressed 10 times)

mainly along bedding planes of No.1 and No.2 continuously, and sliding surfaces are formed at last. Massive rock masses slide along No.2 bedding plane with certain displacement, meanwhile there is also dislocation occurred along No.1 bedding plane, as shown in Fig. 12(b). As a result, cascaded settlement occurs at the crest of the slope, as illustrated in Fig. 12. Main sliding masses still remain on the slope, and small rock falls occur and accumulate at the slope toe (see Fig. 13(a)). Additionally, it has been observed that some blocks at the toe are lifted up slightly and formed small cavities due to rock mass sliding along No.3 bedding plane passing through the toe, as shown in the enlarged area in Fig. 12(a). Typical failure phenomena of Stage III are shown in Fig. 13. Furthermore, one of the typical Wenchuan earthquake-induced landslides, Tangjiashan landslide, is shown in Fig. 14. Sliding striation indicated that the majority of rock masses were sliding on the bedding plane. Hence, physical modeling results were consistent with the field investigation and reproduced the mechanism of this kind of geohazard.

Stage IV: as the amplitudes of the accelerations are larger than 0.45 g, many cracks generate, especially in the region above No.3 bedding plane and slope surface, while the farthest locations of cracks are same as that in Stage III, as shown in Fig. 15(a). Meanwhile, those existed cracks in Stage III continue to expand and propagate into the inner slope. As a

result, new sliding surface are mainly formed along No.3 bedding plane and massive rock masses slide along the No.3 bedding plane. Considerable displacement is also observed along the No.2 bedding plane and dislocations among blocks occur along No.1 bedding plane. Conclusively, the slope surface above one third of the slope height is shattered and some tension troughs are observed with depths of ~12 cm (see Fig. 16(a)), and massive fall down rock masses accumulate at the slope toe (see Fig. 16(b)). In addition, the No.4 bedding plane is buckled in the region near slope toe, marked in enlarged rectangular in Fig. 15, and this phenomenon is also observed in postearthquake investigations (Chigira et al. 2003; Chigira et al. 2010; Qi et al. 2015), as shown in Fig. 17, one example of buckling failure triggered by the Wenchuan earthquake.

Discussion

To reduce the boundary effect, absorber material damping liquid was utilized and model size criteria was followed by Lin and Wang (2006). Results showed that acceleration monitoring data was distributed in a reasonable range and little deformation observed at the boundary of the model. Hence, the rigid box boundary effect had little effect on the wave transmission at the rear of the slope. Furthermore, the progressive failure of the slope under earthquake

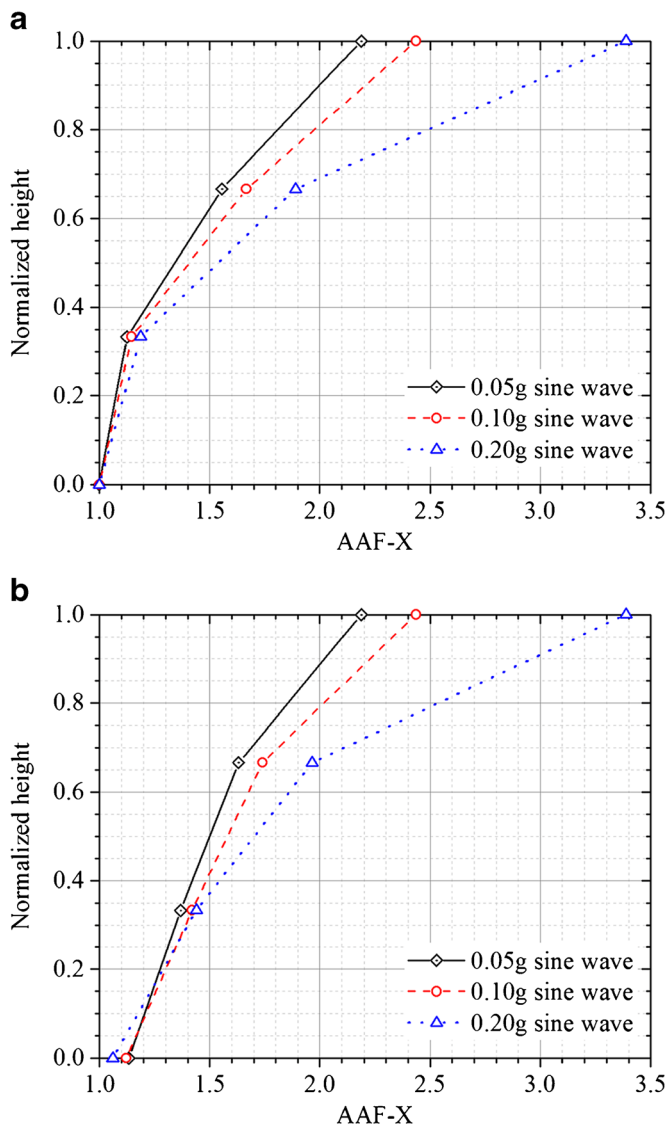


Fig. 7 The AAF-X under sine wave excitation with frequency of 30 Hz and varied amplitudes of 0.05 g, 0.1 g, and 0.2 g: **a** along the slope surface and **b** along section V1

was consistent with the postearthquake geohazard investigations and the formation mechanism of bedding plane slope appeared to be substantiated by the physical test.

Rock mass effect on seismic response of the slope

Significantly, model test results revealed that strong seismic response was amplified at the slope surface and crest, which concurred with homogeneous physical model results (Lin and Wang 2006; Wang and Lin 2011) and also confirmed previous findings of the research group (Yang et al. 2018; Zhan et al. 2019b). Solid field earthquake monitoring data also demonstrated topographic amplification effect (Davis and West 1973; Luo et al. 2014; Wang et al. 2017). Especially, the PGAs recorded at a ridge on the left abutment of Pacoima Dam and the crest of Tarzana were 1.58 g and 1.93 g, respectively (Sepulveda et al. 2005; Spudich et al. 1996).

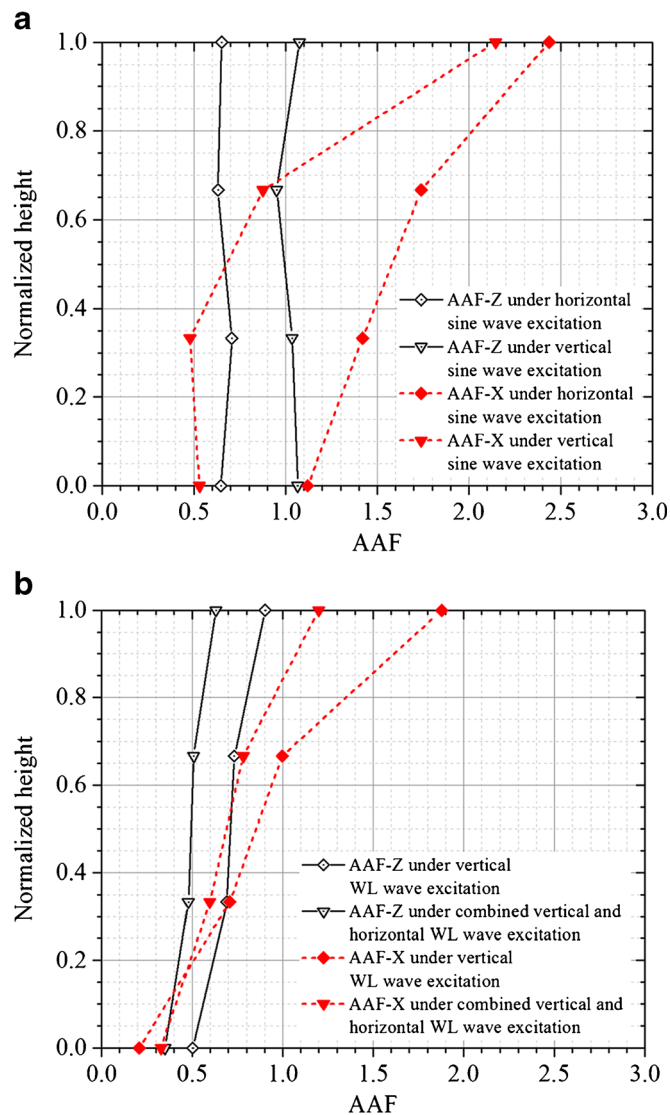


Fig. 8 The AAF along the vertical section V1: **a** horizontal and vertical sine wave excitation with frequency of 30 Hz and amplitude 0.1 g, respectively; **b** vertical WL and XZ WL wave excitations with amplitude 0.1 g

Simultaneously, numerical simulations results (Bouckovalas and Papadimitriou 2005; Li et al. 2019a; Qi et al. 2003), were also in keeping with modeling tests. In addition, the existence of bedding plane in the model slope intensified the seismic response amplification at the slope surface and crest compared with the homogeneous slope (Zhan et al. 2019b) or antidip rock slope (Yang et al. 2018), due to cyclic wave transmission and reflection through bedding planes, which was also found in recent researches. Consequently, the maximum AAF-X of the contour map would cover a larger range and expand to a deeper depth below the slope surface. Figure 6(e) presents the evidence that seismic response amplification was obvious along the bedding plane and it indicated that the isoline of AAF-X was nearly parallel to the bedding planes, which might result in massive movement of rock mass along the bedding plane under stronger earthquake intensity. Furthermore, the existent of vertical acceleration, especially near-field site, proved to

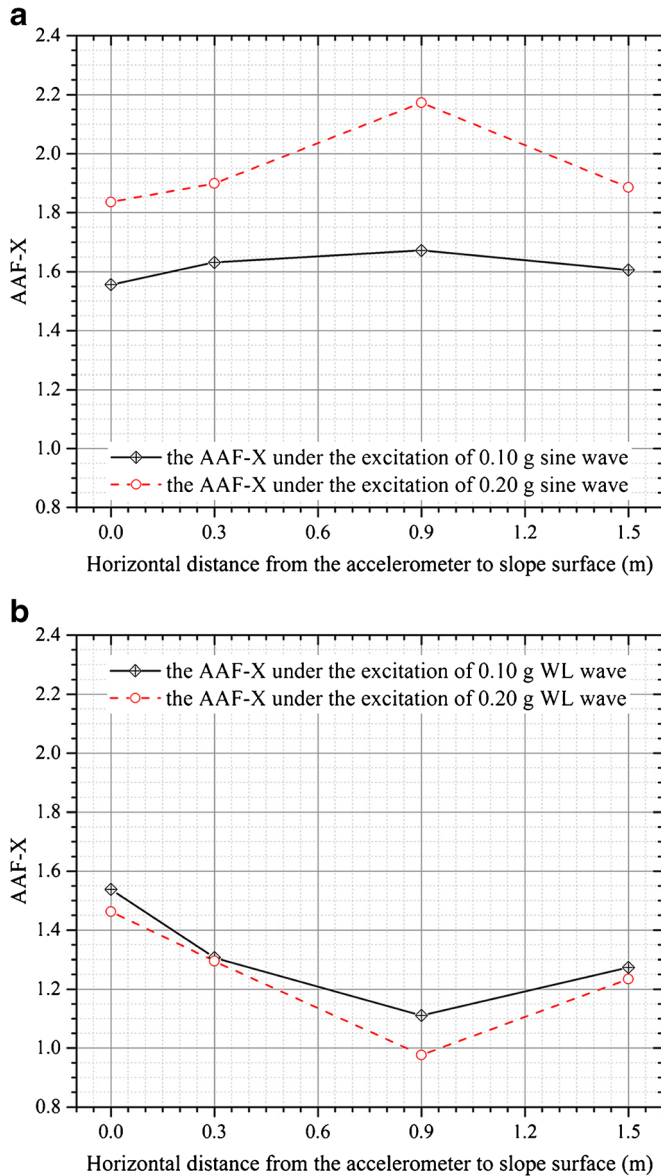


Fig. 9 The AAF-X along the section H2: **a** horizontal sine wave excitation with frequency of 30 Hz and varied amplitudes of 0.1 g and 0.2 g and **b** XZ WL wave excitation with amplitudes of 0.1 g and 0.2 g (compressed 5 times)

have a contribution to initiation and displacement of a landslide (Malla 2017; Shinoda et al. 2013; Wang and Lin 2011). Physical model results also demonstrated that vertical accelerations at the slope toe and crest maintained a considerable value compared with that at shaking table base, as depicted in Fig. 18(a). The ratios of the PGA in vertical to horizontal (R_{Z-X}) under horizontal excitations and ZX excitations when amplitudes were below 0.3 g (a total of 20 IEs listed in Table 6), were calculated along the slope surface, as shown in Fig. 18(b). It can be found that the R_{Z-X} had a decreased tendency with the increase of the slope elevation along the slope surface and the average of the R_{Z-X} was greater than 1 when the normalized height was less than 1/3. Because the topography and bedding plane will reduce the horizontal constraint significantly while slightly in vertical, seismic response in

horizontal showed an increase tendency while in vertical showed an attenuation law. Hence, the R_{Z-X} will decrease with the increase of the slope elevation. Additionally, shear failure was initiated at the lower part of the slope due to vertical acceleration reducing the normal stress of the slope, while tensile failure will occur first at the crest of the slope because of considerable horizontal ground motion.

In this study, the site response was characterized by recorded PGA or average value at various locations as follows: a_{fft} , the maximum free-field acceleration in front of the toe, was defined as the average peak absolute acceleration of A02 and A03; a_{ffc} , the maximum free-field acceleration behind the crest, was defined as the average peak absolute acceleration of A12, A27, and A28; and a_{max} , the maximum crest acceleration, was peak absolute acceleration of A07. Hence, three measures of amplifications, i.e., topographic amplification A_t ($A_t = \frac{a_{max} - a_{ffc}}{a_{ffc}}$), site amplification A_s ($A_s = \frac{a_{ffc} - a_{fft}}{a_{fft}}$) and apparent amplification A_a ($A_a = \frac{a_{max} - a_{fft}}{a_{fft}}$) were computed, proposed by Ashford and Sitar (1997). Table 7 indicates that A_s was 7.65–9.85 times greater than A_t while A_a was 1.19–1.31 times greater than A_s . It concluded that site conditions including material and rock mass structure determined the seismic response amplification at the crest of the slope, while topography just intensified ground motion in this case study, which was also supported by recent field monitoring data and numerical simulation results (He et al. 2020).

Nonlinear dynamic response

It was found that bedding planes had an important effect on the seismic response of the slope when the input amplitudes were less than 0.3 g as described in the “Rock mass effect on seismic response of the slope” section. Meanwhile, the characteristics of the input motions also had profound effects on the seismic response of the slope. It indicated that the seismic response of the slope under sine wave was stronger than that under WL waves as shown in Fig. 6 (b), (d), (e), and (f). This was caused by interaction between the dynamic characteristics of the slope and input motion spectral characteristics. The frequency of the sine wave was around the slope resonance frequency and the slope showed stronger seismic response. Hence, more attention should be paid to input motion spectral characteristics on seismic response of the slope under same amplitude. Nevertheless, with the increase of input amplitude during physical modeling test process, nonlinear dynamic response of the slope was observed. Figure 19(a) clearly indicates that the AAF-X along the slope surface and behind the crest increased first when the input amplitude was below 0.2 g, and then decreased with increase of the input amplitude which also corresponded to different progressive failure at stages I, II, and III. Although the input frequency at stage II was 20 Hz, not 30 Hz, and different from other stages, deformation observed at the slope surface still supported weakening dynamic response at the crest of the slope. The nonlinear phenomenon can be explained as follows: the geometry and rock mass simultaneously resulted in a considerable PGA near the slope crest area and the rock mass was under cyclic tensile-shear force or compressive-shear force; also, the stronger the ground motion intensity, the greater the damage of rock mass and slope structure, like the tension and shear cracks propagated in Fig. 11; in addition, the weaker structure will dissipate more energy which directly led to decrease of

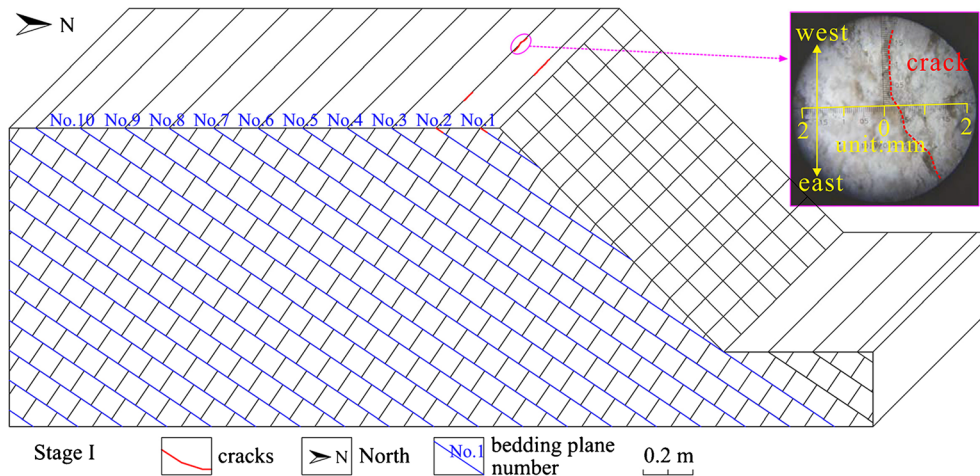


Fig. 10 Stage I: no obvious deformation occurs and only a few tensile cracks initiate between the blocks at the crest of the slope primarily along bedding planes of No.1 and No.2, when the input shaking intensities are less than 0.2 g

dynamic response as shown in Fig. 19(b) (the PGA near the surface under 0.3 g amplitude was smaller than that under 0.2 g); thus, the seismic response at certain location would show nonlinear dynamic response, when the dissipated energy was more than the ground motion amplification. To some extent, surficial loose rock masses will amplify the seismic response of the slope, like the stage III in Fig. 19(a) and PGA along the surface under amplitude 0.45 g in Fig. 19(b). Nonetheless, when the rock masses or rock mass structures were in plastic or inelastic state, the seismic response of the slope would tend to be more complex (increasing AAF-X from Stage II to Stage III at the upper part of the slope surface, as shown in Fig. 19), under the combined effect of input motion characteristics, geometry and rock mass of the slope.

Meanwhile, recorded acceleration time-histories of input motion, at slope toe, crest, and behind the crest are shown in Fig. 20 (using the Butterworth bandpass filter 20–40 Hz in MATLAB). It indicated that the shape of the waveform at the slope crest was significantly different from others while other parts of the slope

were consistent with input motion. It also showed that shear and tension cracks were initiated at the upper part of the slope at 1s in Fig. 20(c). Then, those cracks were propagated at 2s as shown in Fig. 20(d). From 1 to 2s, the acceleration at A07 showed a sharp decrease, which presented nonlinear characteristics at the slope crest due to deterioration of rock masses. Finally, rock masses were sliding along the bedding plane with time, in Fig. 20(e), (f), and (g). Hence, the failed rock masses had an important effect on the seismic response of the slope. In turn, nonlinear seismic response of the slope will affect the failure evolution progress of the slope as well.

Implication to engineering

Nowadays, few seismic codes or provisions consider topographic amplification in rock slope engineering. Eurocode-8 provisions (2008) recommended topographic amplification factor for different cases as follows: (a) amplification factor is 1.0, when slopes are lower than 15° or the relative height of the slope < 30m; (b)

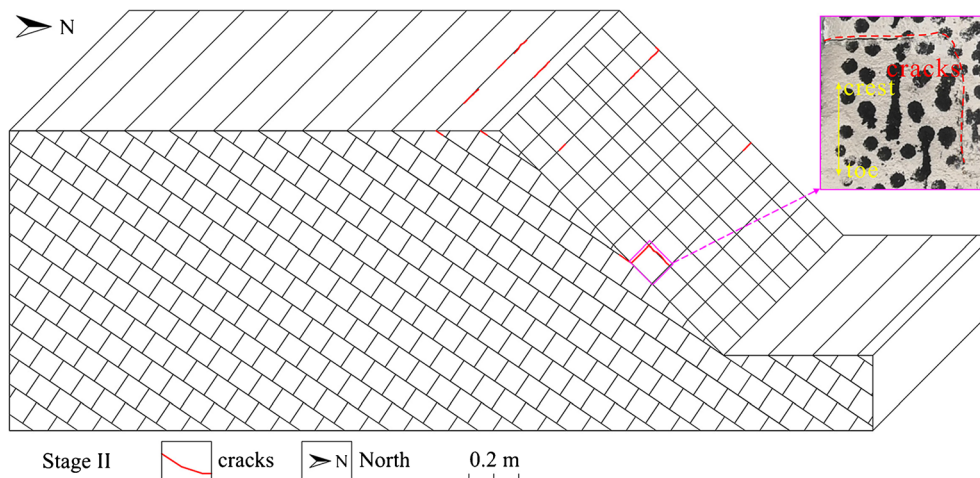


Fig. 11 Stage II: as amplitude is 0.3 g, existing cracks continue to grow and several shear cracks present at the slope surface above one third of the slope height along bedding planes of No.1 and No.2

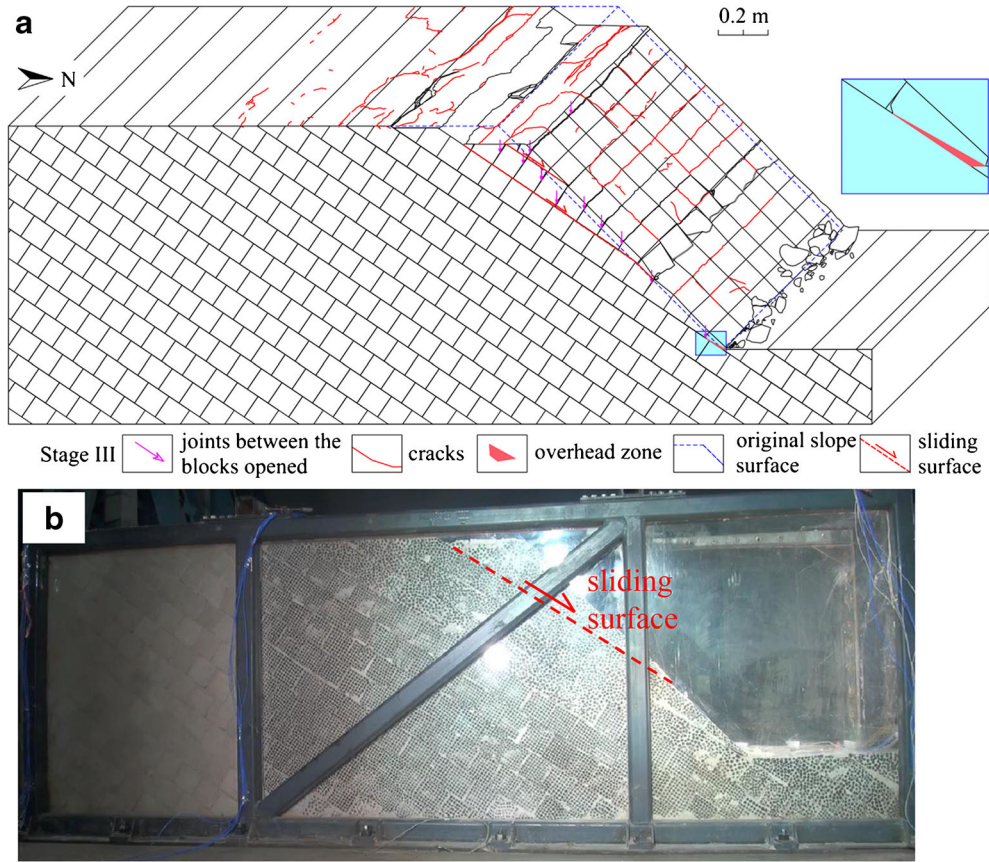


Fig. 12 Stage III: when the shaking amplitude of the acceleration reaches 0.45 g, cracks grow along the second bedding plane continuously, and sliding surfaces are mainly formed and massive rock masses are sliding along the No.1 and No.2 bedding planes.

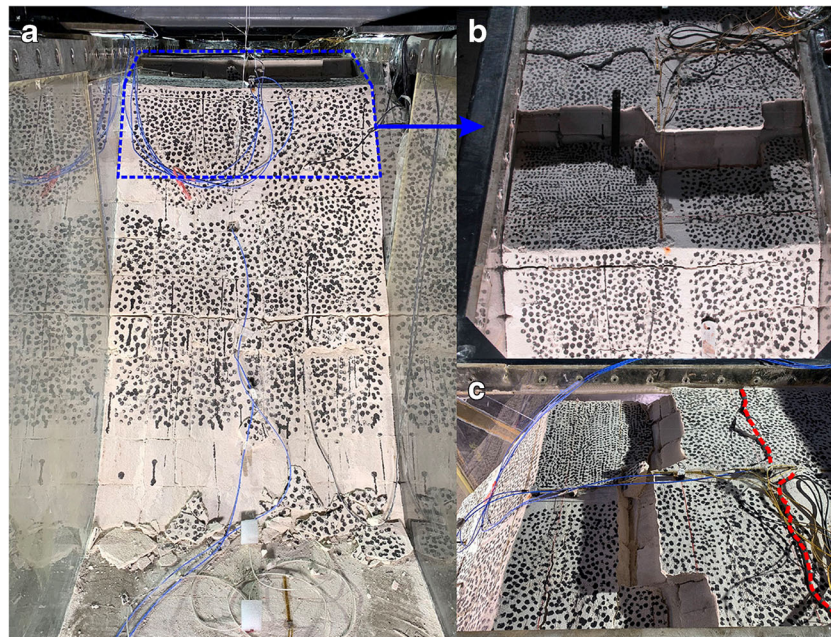


Fig. 13 a Failure at the surface of the slope, b the sliding surface at the crest of the slope, and c the sliding surface and cracks at the crest from the west side view

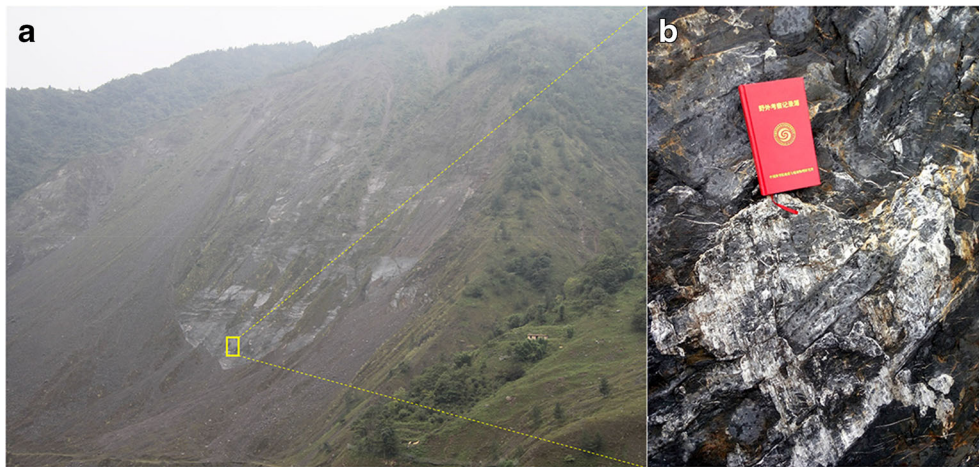


Fig. 14 a Tangjiashan landslide triggered by Wenchuan earthquake and b sliding surface along the bedding plane

amplification factor is equal to 1.2, when slopes are between 15° and 30° and the relative height of the slope $> 30\text{m}$; and (c) amplification factor is 1.4 when slopes are steeper than 30° and the relative height of the slope $> 30\text{m}$. Nonetheless, the

amplification factor at the slope crest in this study is close to 3.4 (Fig. 6(c) and Fig. 7) which is almost 2.4 times larger than that proposed by Eurocode-8 provisions. More importantly, amplification factors vary with different input frequencies or excitation

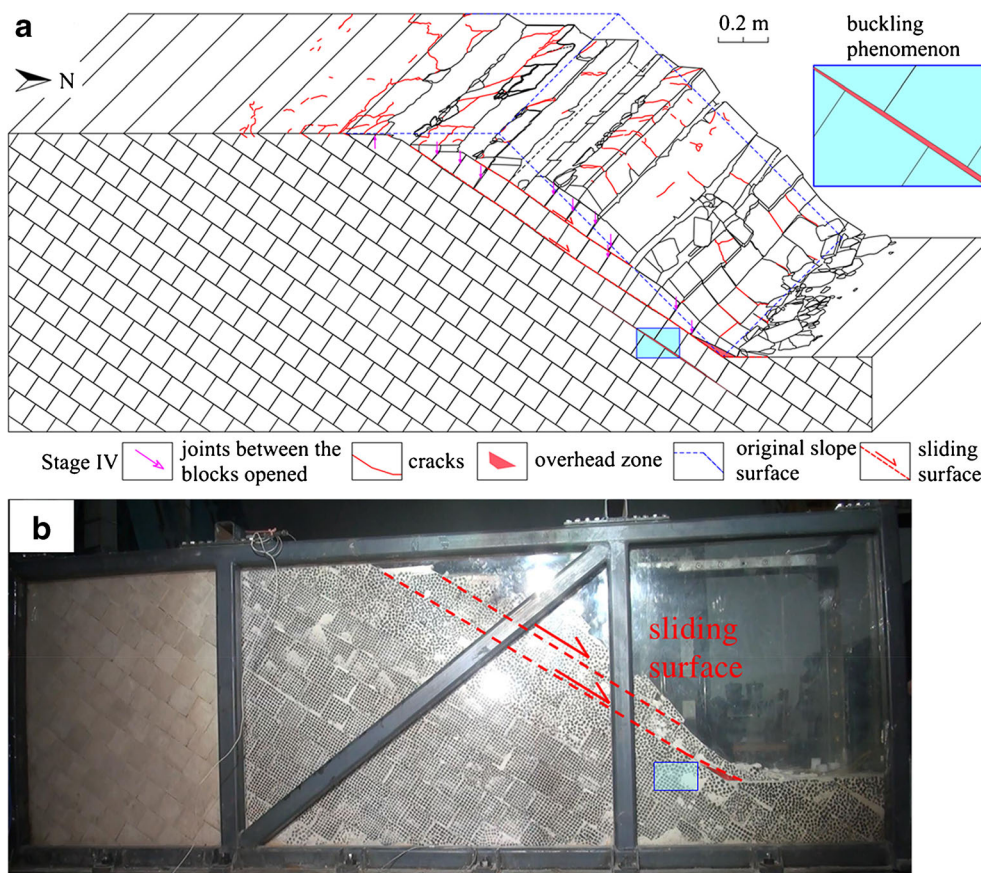


Fig. 15 Stage IV: as the amplitudes of the accelerations are larger than 0.45 g, cracks are propagated and connected in inner slope, and new sliding surfaces are mainly formed along the No.3 bedding plane and rock masses fall down from upper part of the slope

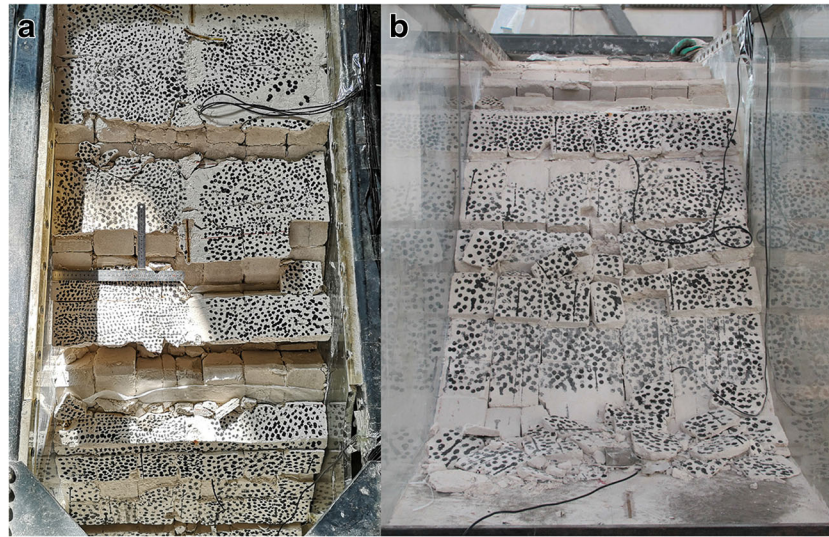


Fig. 16 The final “step-like” failure morphology at the surface of the slope: **a** from top view and **b** from the north side



Fig. 17 Buckling failure triggered by Wenchuan earthquake (Qi et al. 2015)

directions. It can be found that the seismic design parameters may be conservative or unconservative for bedding rock slope engineering. Hence, coupling effect of rock mass structure and seismic characteristics should be considered in seismic design of slope engineering, especially in active seismic mountainous areas, like south-west of China. At the same time, more works should be taken to study the seismic response of the rock slope using physical modeling and numerical simulations.

Conclusions

In this study, a large-scale rock slope was constructed contained bedding planes dipped out of the surface, to conduct a series of shaking table tests considered different amplitudes and frequency spectrum characteristics. The accelerations at various locations were recorded and deformation characteristics was observed in detail under each excitation. In summary, some significant findings can be reached as follows:

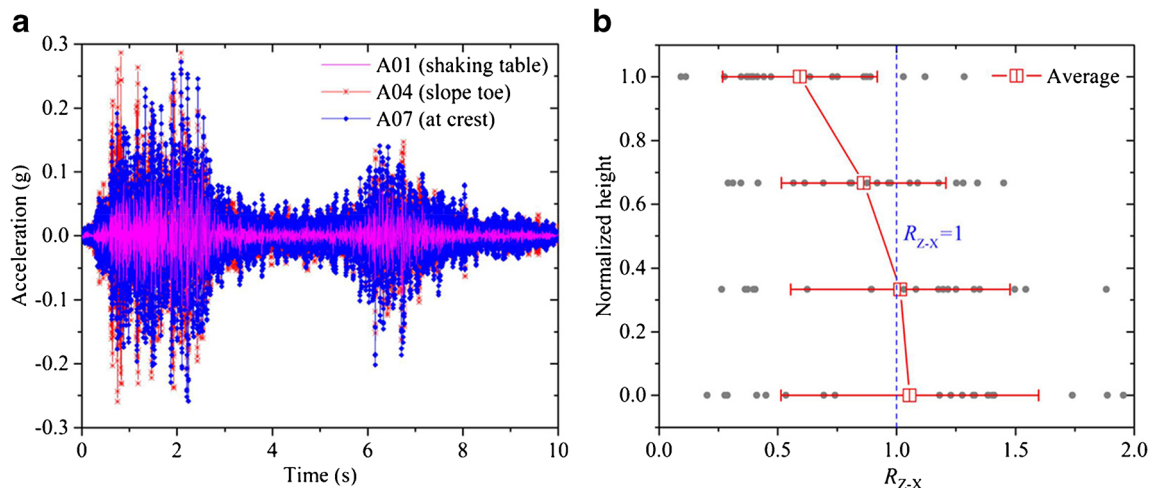


Fig. 18 **a** The recorded vertical acceleration under WL excitation (IE34 in Table 6) and **b** R_{z-x} along the slope surface

Table 7 Calculated A_b , A_s , and A_a under different IEs

Excitation	a_{fft} (g)	a_{ffc} (g)	a_{max} (g)	A_t (%)	A_s (%)	A_a (%)
IE03	0.05	0.09	0.10	8.42	82.93	98.34
IE23	0.11	0.21	0.23	11.26	95.86	117.91
IE28	0.21	0.56	0.67	19.60	166.70	218.98
IE38	0.58	1.19	1.36	13.94	106.70	135.52

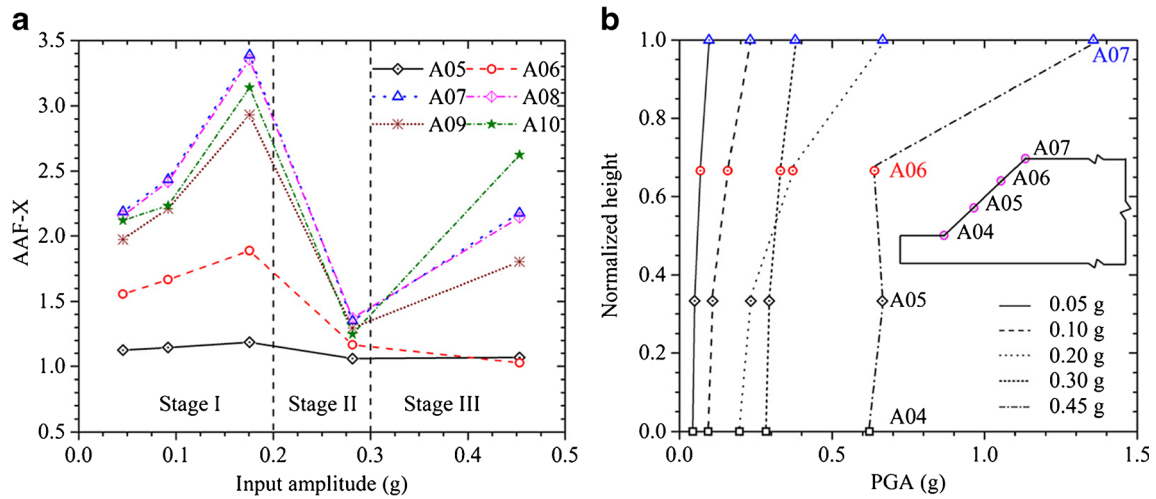


Fig. 19 The AAF-X at different position along the slope surface under different input amplitude (IE03, IE23, IE28, IE37, and IE38 in Table 5)

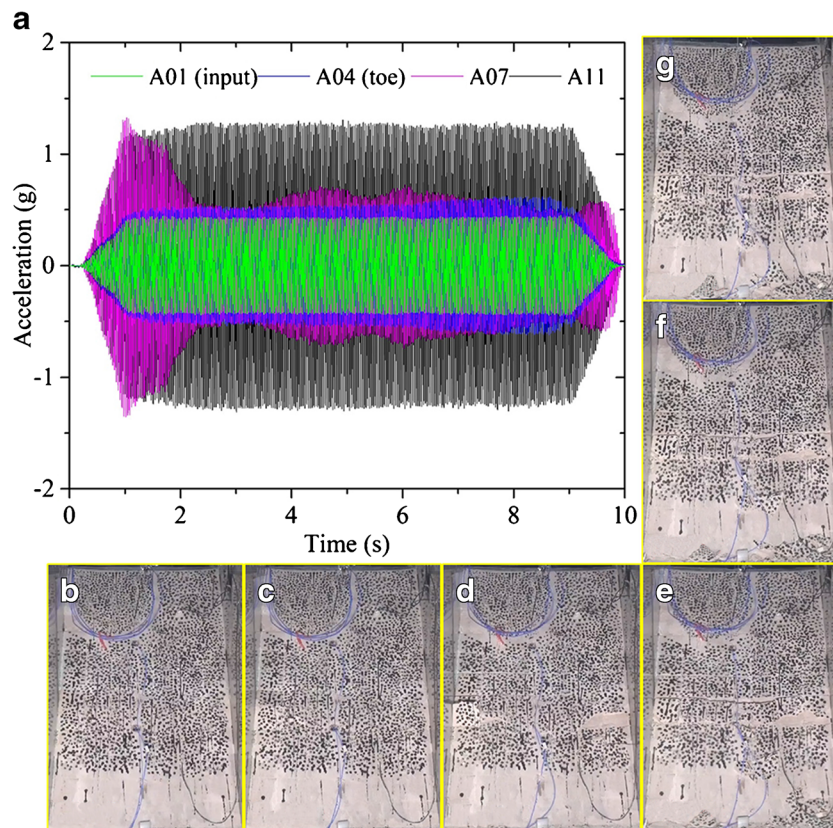


Fig. 20 Recorded acceleration time-histories and failure evolution at the slope surface under IE38 excitation

- (1) Seismic response of the slope is amplified at crest and surface of the slope. The AAF-X is obviously amplified at the middle and upper part of the slope surface, while the AAF-Z shows stronger amplification at lower part of the slope. The AAF-X under horizontal direction excitation is larger than that under vertical excitation and AAF-Z under vertical excitation is larger than that under horizontal excitation. The existence of bedding planes makes isoline of AAF-X nearly parallel to the bedding plane near the surface of the slope, which will lead to massive movement of rock mass under stronger earthquake intensity. The combination of rock mass structure and topography results in strong seismic response and rock mass dominates the seismic response at the crest.
- (2) The AAF-X increases with the increase of the shaking intensity in elastic state. When the input excitation amplitude was greater than 0.2 g, the slope crest and surface began to show nonlinear dynamic response. This could be explained by the fact that the stronger the ground motion intensity, the greater the damage of rock mass and the weaker structure of the slope would dissipate more energy. Therefore, when the dissipated energy was beyond ground motion amplification, the dynamic response at certain location of the slope would show nonlinear dynamic response.
- (3) Through detailed description and sketch of cracks and deformations of the slope, the progressive failure evolution of the slope can be characterized by four stages: stage I, no obvious deformation occurs and only few tension cracks initiate between the blocks with openness less than 0.1 mm at the crest of the slope primarily; stage II, existing cracks grow continuously and several shear cracks initiate above one third of the slope height along bedding planes of No.1 and No.2; stage III, the cracks grow along the bedding plane continuously and massive rock masses mainly slide along the No.2 bedding plane; stage IV, cracks propagate and coalesce in depth resulting in new sliding surface (No.3 bedding plane) formed in depth, and the final failure morphology is “step-like” at the surface of the slope. Those failure evolutions can reproduce typical bedding plane failure and buckling failure during the Wenchuan earthquake.

Acknowledgements

The authors wish to acknowledge financial support from the National Natural Science Foundation of China under grants of 41825018, 41672307, and 41790442, and Institute of Geology and Geophysics, Chinese Academy of Sciences under grant of KLSG201709. The authors also would like to express their gratitude to Drs. Li Chunlei and Xu Lianghua of Earthquake Engineering Research Center, China Institute of Water Resources and Hydro-power Research, for their helpful advice.

References

Ashford SA, Sitar N (1997) Analysis of topographic amplification of inclined shear waves in a steep coastal bluff. *Bull Seismol Soc Am* 87:692–700

Bhasin R, Kaynia AM (2004) Static and dynamic simulation of a 700-m high rock slope in western Norway. *Eng Geol* 71:213–226. [https://doi.org/10.1016/s0013-7952\(03\)00135-2](https://doi.org/10.1016/s0013-7952(03)00135-2)

Bouchon M, Barker JS (1996) Seismic response of a hill: the example of Tarzana, California. *Bull Seismol Soc Am* 86:66–72

Bouckovalas GD, Papadimitriou AG (2005) Numerical evaluation of slope topography effects on seismic ground motion. *Soil Dyn Earthq Eng* 25:547–558. <https://doi.org/10.1016/j.soildyn.2004.11.008>

Brand L (1957) The Pi-theorem of dimensional analysis. *Arch Ration Mech Anal* 1:35–45. <https://doi.org/10.1007/bf00297994>

Buckingham E (1914) On physically similar systems, illustrations of the use of dimensional equations. *Phys Rev* 4:345–376. <https://doi.org/10.1103/PhysRev.4.345>

Chigira M, Wang W-N, Furuya T, Kamai T (2003) Geological causes and geomorphological precursors of the Tsaoling landslide triggered by the 1999 Chi-Chi earthquake, Taiwan. *Eng Geol* 68:259–273

Chigira M, Wu XY, Inokuchi T, Wang GH (2010) Landslides induced by the 2008 Wenchuan earthquake, Sichuan, China. *Geomorphology* 118:225–238. <https://doi.org/10.1016/j.geomorph.2010.01.003>

Collier CJ, Elashai AS (2001) A procedure for combining vertical and horizontal seismic action effects. *J Earthq Eng* 5:521–539. <https://doi.org/10.1142/s136324690100056x>

Curtis WD, Logan JD, Parker WA (1982) Dimensional analysis and the Pi-theorem. *Linear Algebra Appl* 47:117–126. [https://doi.org/10.1016/0024-3795\(82\)90229-4](https://doi.org/10.1016/0024-3795(82)90229-4)

Davis LL, West LR (1973) Observed effects of topography on ground motion. *Bull Seismol Soc Am* 63:283–298

Fan G, Zhang JJ, Wu JB, Yan KM (2016) Dynamic response and dynamic failure mode of a weak intercalated rock slope using a shaking table. *Rock Mech Rock Eng* 49:3243–3256. <https://doi.org/10.1007/s00603-016-0971-7>

Fan G, Zhang LM, Zhang JJ, Yang CW (2017) Time-frequency analysis of instantaneous seismic safety of bedding rock slopes. *Soil Dyn Earthq Eng* 94:92–101. <https://doi.org/10.1016/j.soildyn.2017.01.008>

Fan G, Zhang LM, Zhang JJ, Yang CW (2019) Analysis of seismic stability of an obsequent rock slope using time-frequency method. *Rock Mech Rock Eng* 52:3809–3823. <https://doi.org/10.1007/s00603-019-01821-9>

Finn WDL, Ventura CE, Schuster ND (1995) Ground motions during the 1994 Northridge earthquake. *Can J Civ Eng* 22:300–315. <https://doi.org/10.1139/1995-044>

Graizer V (2009) Low-velocity zone and topography as a source of site amplification effect on Tarzana hill, California. *Soil Dyn Earthq Eng* 29:324–332. <https://doi.org/10.1016/j.soildyn.2008.03.005>

Guo SF, Qi SW, Yang GX, Zhang SS, Saroglou C (2017) An analytical solution for block toppling failure of rock slopes during an earthquake. *Appl Sci-Basel* 7:17. <https://doi.org/10.3390/app7101008>

He J, Qi S, Wang Y, Saroglou C (2020) Seismic response of the Lengzhuguan slope caused by topographic and geological effects. *Eng Geol* 265:105431. <https://doi.org/10.1016/j.enggeo.2019.105431>

Hoek E, Bray JD (1981) *Rock slope engineering*. CRC Press

Huang RQ, Zhao JJ, Ju NP, Li G, Lee ML, Li YR (2013) Analysis of an anti-dip landslide triggered by the 2008 Wenchuan earthquake in China. *Nat Hazards* 68:1021–1039. <https://doi.org/10.1007/s11069-013-0671-5>

Iai S (1989) Similitude for shaking table tests on soil-structure-fluid model in 1g gravitational field. *Soils Found* 29:105–118

Li HH, Lin CH, Zu W, Chen CC, Weng MC (2018) Dynamic response of a dip slope with multi-slip planes revealed by shaking table tests. *Landslides* 15:1731–1743. <https://doi.org/10.1007/s10346-018-0992-2>

Li HB, Liu YQ, Liu LB, Liu B, Xia X (2019a) Numerical evaluation of topographic effects on seismic response of single-faced rock slopes. *Bull Eng Geol Environ* 78:1873–1891. <https://doi.org/10.1007/s10064-017-1200-7>

Li LQ, Ju NP, Zhang S, Deng XX (2019b) Shaking table test to assess seismic response differences between steep bedding and toppling rock slopes. *Bull Eng Geol Environ* 78:519–531. <https://doi.org/10.1007/s10064-017-1186-1>

Li LQ, Ju NP, Zhang S, Deng XX, Sheng DC (2019c) Seismic wave propagation characteristic and its effects on the failure of steep jointed anti-dip rock slope. *Landslides* 16:105–123. <https://doi.org/10.1007/s10346-018-1071-4>

Lin ML, Wang KL (2006) Seismic slope behavior in a large-scale shaking table model test. *Eng Geol* 86:118–133. <https://doi.org/10.1016/j.enggeo.2006.02.011>

Liu HX, Xu Q, Li YR, Fan XM (2013) Response of high-strength rock slope to seismic waves in a shaking table test. *Bull Seismol Soc Am* 103:3012–3025. <https://doi.org/10.1785/0120130055>

Liu HX, Xu Q, Li YR (2014) Effect of lithology and structure on seismic response of steep slope in a shaking table test. *J Mt Sci* 11:371–383. <https://doi.org/10.1007/s11629-013-2790-6>

Liu DZ, Cui YF, Guo J, Yu ZL, Chan D, Lei MY (2020) Investigating the effects of clay/sand content on depositional mechanisms of submarine debris flows through physical and numerical modeling. *Landslides* 17:1863–1880. <https://doi.org/10.1007/s10346-020-01387-6>

- Luo YH, Del Gaudio V, Huang RQ, Wang YS, Wasowski J (2014) Evidence of hillslope directional amplification from accelerometer recordings at Qiaozhuang (Sichuan - China). *Eng Geol* 183:193–207. <https://doi.org/10.1016/j.enggeo.2014.10.015>
- Malla S (2017) Consistent application of horizontal and vertical earthquake components in analysis of a block sliding down an inclined plane. *Soil Dyn Earthq Eng* 101:176–181. <https://doi.org/10.1016/j.soildyn.2017.06.008>
- Meymand P (1998) Shaking table scale model tests of nonlinear soil-pile-superstructure interaction in soft clay.
- Pelekis P, Batilas A, Pefani E, Vlachakis V, Athanasopoulos G (2017) Surface topography and site stratigraphy effects on the seismic response of a slope in the Achaia-Illia (Greece) 2008 M(w)6.4 earthquake. *Soil Dyn Earthq Eng* 100:538–554. <https://doi.org/10.1016/j.soildyn.2017.05.038>
- Qi SW, Wu FQ, Sun JZ (2003) General regularity of dynamic responses of slopes under dynamic input. *Sci China Ser E Eng Mater Sci* 46:120–132. <https://doi.org/10.1360/03ez0006>
- Qi S, Xu Q, Lan H, Zhang B, Liu J (2010) Spatial distribution analysis of landslides triggered by 2008.5. 12 Wenchuan Earthquake, China. *Eng Geol* 116:95–108
- Qi SW, Xu Q, Zhang B, Zhou YD, Lan HX, Li LH (2011) Source characteristics of long runout rock avalanches triggered by the 2008 Wenchuan earthquake, China. *J Asian Earth Sci* 40:896–906. <https://doi.org/10.1016/j.jseae.2010.05.010>
- Qi SW, Xu Q, Lan HX, Zhang B, Liu JY (2012) Resonance effect existence or not for landslides triggered by 2008 Wenchuan earthquake: a reply to the comment by Drs. Xu Chong and Xu Xiwei. *Eng Geol* 151:128–130. <https://doi.org/10.1016/j.enggeo.2012.08.003>
- Qi SW, Lan HX, Dong JY (2015) An analytical solution to slip buckling slope failure triggered by earthquake. *Eng Geol* 194:4–11. <https://doi.org/10.1016/j.enggeo.2014.06.004>
- Sepulveda SA, Murphy W, Jibson RW, Petley DN (2005) Seismically induced rock slope failures resulting from topographic amplification of strong ground motions: the case of Pacoima Canyon California. *Eng Geol* 80:336–348. <https://doi.org/10.1016/j.enggeo.2005.07.004>
- Shi ZM, Wang YQ, Peng M, Guan SG, Chen JF (2015) Landslide dam deformation analysis under aftershocks using large-scale shaking table tests measured by videogrammetric technique. *Eng Geol* 186:68–78. <https://doi.org/10.1016/j.enggeo.2014.09.008>
- Shinoda M, Nakajima S, Nakamura H, Kawai T, Nakamura S (2013) Shaking table test of large-scaled slope model subjected to horizontal and vertical seismic loading using E-Defense. In: Proceedings of the 18th International Conference on Soil Mechanics and Geotechnical Engineering, pp 1603–1606
- Shou KJ, Wang CF (2003) Analysis of the Chiufengershan landslide triggered by the 1999 Chi-Chi earthquake in Taiwan. *Eng Geol* 68:237–250. [https://doi.org/10.1016/s0013-7952\(02\)00230-2](https://doi.org/10.1016/s0013-7952(02)00230-2)
- Song DQ, Che AL, Chen Z, Ge XR (2018a) Seismic stability of a rock slope with discontinuities under rapid water drawdown and earthquakes in large-scale shaking table tests. *Eng Geol* 245:153–168. <https://doi.org/10.1016/j.enggeo.2018.08.011>
- Song DQ, Che AL, Zhu RJ, Ge XR (2018b) Dynamic response characteristics of a rock slope with discontinuous joints under the combined action of earthquakes and rapid water drawdown. *Landslides* 15:1109–1125. <https://doi.org/10.1007/s10346-017-0932-6>
- Spudich P, Hellweg M, Lee WHK (1996) Directional topographic site response at Tarzana observed in aftershocks of the 1994 Northridge, California, earthquake: implications for mainshock motions. *Bull Seismol Soc Am* 86:5193–5208
- Wang KL, Lin ML (2011) Initiation and displacement of landslide induced by earthquake—a study of shaking table model slope test. *Eng Geol* 122:106–114. <https://doi.org/10.1016/j.enggeo.2011.04.008>
- Wang W-N, Chigira M, Furuya T (2003) Geological and geomorphological precursors of the Chiu-fen-erh-shan landslide triggered by the Chi-chi earthquake in central Taiwan. *Eng Geol* 69:1–13
- Wang H, Tu J, Li D (2004) Simulation of radiational damping of unbounded medium in shaking table test. *Journal of Hydraulic Engineering* 39–44
- Wang GH, Huang RQ, Lourenco SDN, Kamai T (2014) A large landslide triggered by the 2008 Wenchuan (M8.0) earthquake in Donghekou area: phenomena and mechanisms. *Eng Geol* 182:148–157. <https://doi.org/10.1016/j.enggeo.2014.07.013>
- Wang YS, He JX, Luo YH (2017) Seismic response of the Lengzhuguan slope during Kangding Ms5.8 earthquake. *J Mt Sci* 14:2337–2347. <https://doi.org/10.1007/s11629-017-4368-1>
- Wartman J, Seed RB, Bray JD (2005) Shaking table modeling of seismically induced deformations in slopes. *J Geotech Geoenviron* 131:610–622. [https://doi.org/10.1061/\(asce\)1090-0241\(2005\)131:4\(610\)](https://doi.org/10.1061/(asce)1090-0241(2005)131:4(610))
- Xu WJ, Xu Q, Wang YJ (2013) The mechanism of high-speed motion and damming of the Tangjiashan landslide. *Eng Geol* 157:8–20. <https://doi.org/10.1016/j.enggeo.2013.01.020>
- Yan Y, Cui Y, Tian X, Hu S, Guo J, Wang Z, Yin S, Liao L (2020) Seismic signal recognition and interpretation of the 2019 "7.23" Shuicheng landslide by seismogram stations. *Landslides* 17:1191–1206. <https://doi.org/10.1007/s10346-020-01358-x>
- Yang G, Qi S, Wu F, Zhan Z (2018) Seismic amplification of the anti-dip rock slope and deformation characteristics: a large-scale shaking table test. *Soil Dyn Earthq Eng* 115:907–916. <https://doi.org/10.1016/j.soildyn.2017.09.010>
- Yang G, Ye H, Wu F, Qi S, Dong J (2012) Shaking table model test on dynamic response characteristics and failure mechanism of antidip layered rock slope. *Chin J Rock Mech Eng* 31:2214–2221
- Yin YP, Wang FW, Sun P (2009) Landslide hazards triggered by the 2008 Wenchuan earthquake, Sichuan, China. *Landslides* 6:139–152. <https://doi.org/10.1007/s10346-009-0148-5>
- Yuan RM, Tang CL, Hu JC, Xu XW (2014) Mechanism of the Donghekou landslide triggered by the 2008 Wenchuan earthquake revealed by discrete element modeling. *Nat Hazards Earth Syst Sci* 14:1195–1205. <https://doi.org/10.5194/nhess-14-1195-2014>
- Zhan ZF, Qi SW (2017) Numerical study on dynamic response of a horizontal layered-structure rock slope under a normally incident Sv wave. *Appl Sci-Basel* 7:16. <https://doi.org/10.3390/app7070716>
- Zhan Z, He J, Zheng B, Qi S (2019a) Experimental study on similar material proportion of slope model. *Prog Geophys* 34:1236–1243
- Zhan Z, Qi S, He N, Zheng B, Ge C (2019b) Shaking table test study of homogeneous rock slope model under strong earthquake. *J Eng Geol* 27:946–954
- Zhang M, Yin YP, McSaveney M (2016) Dynamics of the 2008 earthquake-triggered Wenjiagou Creek rock avalanche, Qingping, Sichuan, China. *Eng Geol* 200:75–87. <https://doi.org/10.1016/j.enggeo.2015.12.008>
- Zhang ZZ, Fleurisson JA, Pellet F (2018) The effects of slope topography on acceleration amplification and interaction between slope topography and seismic input motion. *Soil Dyn Earthq Eng* 113:420–431. <https://doi.org/10.1016/j.soildyn.2018.06.019>

J. He · S. Qi · S. Guo · B. Zheng · X. Huang · Y. Zou · N. Liang

Key Laboratory of Shale Gas and Geoengineering, Institute of Geology and Geophysics, Chinese Academy of Sciences, Beijing, 100029, China

J. He · S. Qi · S. Guo · B. Zheng · X. Huang · Y. Zou · N. Liang

University of Chinese Academy of Sciences, Beijing, 100049, China

J. He · S. Qi (✉) · S. Guo · B. Zheng · X. Huang · Y. Zou · N. Liang

Innovation Academy for Earth Science, CAS, Beijing, 100029, China
Email: qishengwen@mail.iggcas.ac.cn

Z. Zhan

China Highway Engineering Consultants Corporation, Beijing, 100089, China

C. Li

China Institute of Water Resources and Hydropower Research, Beijing, 100038, China

G. Yang

China University of Geoscience, Beijing, 100083, China